STRUCTURAL CONTROL AND HEALTH MONITORING
Struct. Control Health Monit. 2013; **20**:971–986
Published online 6 August 2012 in Wiley Online Library (wileyonlinelibrary.com). DOI: 10.1002/stc.1510

Energy-efficient deployment strategies in structural health monitoring using wireless sensor networks

Tat S. Fu[1,*,†], Amitabha Ghosh[2], Erik A. Johnson[3] and Bhaskar Krishnamachari[4]

[1]*Department of Civil Engineering, University of New Hampshire, Durham, NH 03824, U.S.A.*
[2]*Department of Electrical Engineering, Princeton University, Princeton, NJ 08544, U.S.A.*
[3]*Sonny Astani Department of Civil and Environmental Engineering, The University of Southern California, Los Angeles, CA 90089, U.S.A.*
[4]*Ming Hsieh Department of Electrical Engineering, University of Southern California, Los Angeles, CA 90089, U.S.A.*

SUMMARY

Structural health monitoring using wireless sensor networks has drawn considerable attention in recent years. The ease of deployment of tiny wireless devices that are coupled with sensors and actuators enhances the data collection process and makes prognostic and preventive maintenance of an infrastructure much easier. In this paper, the deployment problem is considered for finding node locations to reliably diagnose the health of a structure while consuming minimum energy during data collection. A simple shear structure is considered and modal analysis is performed. The example verifies the expectation that placing nodes further apart from each other reduces the mode shape errors but increases the energy consumption during data collection. A min–max, energy-balanced routing tree and an optimal grid separation formulation are proposed that minimize the energy consumption as well as provide fine grain measurements. Copyright © 2012 John Wiley & Sons, Ltd.

Received 25 June 2011; Revised 28 May 2012; Accepted 28 May 2012

KEY WORDS: structural health monitoring; wireless sensor networks; sensor placement; mode shape analysis; eigensystem realization algorithm (ERA); energy-balanced routing

1. INTRODUCTION

The goal of a wireless structural health monitoring (SHM) system [1–7] is to assess structural integrity using wireless sensor networks (WSNs). Reliable wireless SHM systems that can help predict failures in structures through non-destructive diagnosis procedures can have substantial social and economic benefits. The Columbia space shuttle tragedy and the I-35W Mississippi River bridge collapse have underlined the importance and necessity of reliable monitoring systems in analyzing structural damage and deterioration processes. Typical structural safety assessment depends on visual inspection, which is manual, expensive, and time consuming. Moreover, damage can be *hidden* inside structural elements. With the use of sensors, SHM systems can examine the structural integrity in an automatic and efficient manner. However, installation of wired sensors is expensive, especially in existing buildings, whereas wireless sensors are inexpensive and easily deployable. With the use of damage identification techniques to measure and process structural responses, a wireless SHM system can collaboratively and accurately diagnose the structural health.

Although use of a WSN reduces wiring costs, it comes with two major limitations in terms of energy and bandwidth. Unlike wired networks, wireless sensor nodes are energy constrained as they rely on onboard batteries. Additionally, wireless channels typically have lower bandwidth compared with

*Correspondence to: Tat S. Fu, Department of Civil Engineering, University of New Hampshire, Durham, NH 03824.
†E-mail: Tat.Fu@unh.edu

wired channels because of the lack of a reliable and dedicated medium. Thus, energy efficiency in the data collection process is an important concern for a wireless SHM system.

Node deployment in a WSN is a crucial problem that depends on two related factors: the number of sensors and their locations. Because the sensor readings need to be exchanged and fused for further processing, all sensor nodes should form a connected network. In this paper, wireless SHM is applied to a simple n-story shear structure where each floor is equipped with an equal number of sensors to measure structural responses. Although many sensors (when appropriately deployed) give accurate measurements and result in higher fidelity estimation, they also incur a high communication cost to exchange a large amount of data. On the other hand, fewer sensors imply a low communication cost, but estimates of structural characteristics could be inaccurate. To understand this relationship between WSNs and SHM in terms of sensor placement, this paper considers two most natural deployment strategies, random and grid placements, and presents simulation results from modal analysis based on the *eigensystem realization algorithm* (ERA) and network energy consumption. With the use of ERA, modal characteristics of a structure are estimated from its responses and then used for damage identification. An energy-balanced routing tree is also constructed for the WSN to realistically estimate the energy consumption.

The rest of the paper is organized as follows. Section 2 discusses related works, whereas Section 3 presents the structural, network, and energy models. Section 4 provides a summary of the ERA, and Section 5 presents simulation results. In Section 6, an energy-balanced routing tree construction algorithm is proposed, and optimal determination of inter-node separation is found that minimizes both mode shape error and energy consumption. Finally, Section 7 summarizes the results and gives directions for future research.

2. RELATED WORK

Recent studies [1,8] and deployments [9–12] of wireless SHM have demonstrated the feasibility of autonomous and continuous structural data collection using a WSN, which is inexpensive and more efficient compared with its wired counterpart [2]. However, in addition to determining the optimal locations of sensor nodes for reliable measurements, the bandwidth and energy constraints on these wireless devices have also underlined the need for addressing energy efficiency in the data collection process.

One of the important factors that affect data collection in wireless SHM is the underlying routing mechanism. The notion of energy-balanced (or, more generally, load-balanced) routing in the networking community is a well-researched problem and is proven to be $\mathcal{NP}$-hard [13]. Huang *et al.* [14] presented two energy-aware, load-balanced routing schemes: the maximum capacity path (MCP) and MCP combined with path switching, where a layered network is constructed and every node selects a shortest path with maximum capacity to the sink, sometimes switching paths to its sibling neighbors in order to share traffic. It is shown that both schemes can achieve improved load sharing and, thereby, increase in-network lifetime. Gao *et al.* [15] presented distributed routing algorithms for wireless networks when all the nodes are located in a narrow strip to minimize latency and achieve a good load balance in terms of energy usage. Spencer and colleagues [16,17] expanded on this work, developing algorithms to employ decentralized approaches in a software framework. Shah *et al.* [18] argued that always using the lowest energy paths may not be optimal from the point of view of network lifetime and long-term connectivity and proposed a technique to occasionally use sub-optimal routing paths to provide substantial gains. A node-centric load balancing scheme is presented by Dai and Han [19] considering the Chebyshev sum metric to evaluate the quality of the routing algorithm. Chatterjee *et al.* [20] presented a distributed scheme in the context of data gathering, where nodes are organized into layers and each node selects a parent from its one-hop neighborhood such that the maximum load stays below a certain threshold. The work presented in this paper differs from the aforementioned in the sense that load balancing is formulated in terms of *min–max* fairness with respect to energy consumption by the nodes coupled with the accuracy of structural characteristics estimated by the nodes.

In addition to energy-balanced routing, reliable routing is another major concern for wireless SHM systems [21–23]. However, communication reliability is outside the scope of this paper; reliable data

DOI: 10.1002/stc

transmission is assumed in this study and the authors analyze the reliability of the system related to SHM purposes only. Additionally, researchers have developed software frameworks (e.g., [24]) for facilitating SHM via wireless sensors; this paper develops a methodology that such a framework could use to incorporate limitations of the sensor hardware and the resulting trade-offs with accuracy and other performance metrics that inevitably arise.

A number of studies examined optimal node placement for identification and control of dynamic structures. Udwadia *et al*. [25,26] proposed a scheme to optimally locate sensors by maximizing the trace or determinant of the Fisher information matrix, which is expressed as a function of selected parameters corresponding to the objective function. Heredia-Zavoni *et al*. [27] extended this approach to capture uncertainty in model updating by minimizing the expected Bayesian loss function with the Fisher information matrix. Kammer [28] evaluated the sensor locations by their contribution to the linear independence of the identified model. Hemez *et al*. [29] extended this independence method in terms of strain energy contribution of the structure. Papadimitriou *et al*. [30] used information entropy as a unique measure to model parameter uncertainty and a Bayesian statistical methodology to find optimum sensor placements. Recently, genetic algorithms have also been used for finding optimum sensor placements (e.g., [30–32]). Early studies had mostly been concerned with observability and controllability of dynamic structures, whereas recent ones have started to tie sensor placements with the quality of damage detection. Cobb *et al*. [33] studied the relationship between sensor placement, measured modes, and the extent of damage localization on flexible structures using modal analysis. Shi *et al*. [34] proposed a scheme to optimize sensor placement according to damage detection based on the eigenvector sensitivity method.

These previous studies focused on placing sensors optimally for structural analysis; however, the sensor *network* was left out. The typical objective in these works was to determine where to place m sensors in an n degree-of-freedom (DOF) system, where usually $m \geq n$, and at least one sensor is located at each DOF. This paper assumes that there are multiple sensors on each floor of a building structure, because wireless sensors are designed for large-scale systems, and considers the deployment problem in terms of both quality of damage detection and energy efficiency in the data collection process.

3. PRELIMINARIES

A structural health monitoring system using a wireless sensor network consists of various components: (1) the structure itself, (2) a carefully deployed set of wireless nodes equipped with sensors (such as accelerometers) that could measure the structural response and relay it over multi-hop wireless communication channels to a sink node, and (3) a set of algorithms that take as inputs the measured responses and calculate one or more metrics that indicate the health of the structure.

3.1. Structural model

A simple civil structure, an n-story rectangular shear structure of length l, width w, and story height h, is considered, as illustrated in Figure 1. It is assumed that all floors are uniform, in that the optimal locations of the nodes on a particular floor can be repeated on each floor so long as there is at least one communication link between nodes located on two adjacent floors. This will enable measurements to be communicated across all the floors of the structure in multiple hops and, finally, to a global sink that can aggregate the information and make reliable diagnosis about the health of the structure. For the simulations herein, the dimension of the structure is taken as length $l = 30.48$ cm (12 in.) by width $w = 20.32$ cm (8 in.) by story height $h = 15.24$ cm (6 in.), which is similar to the scaled building model (Figure 2) considered by Chintalapudi *et al*. [35]. The equations of motion can be expressed

$$\mathbf{M}\ddot{\mathbf{x}} + \mathbf{C}\dot{\mathbf{x}} + \mathbf{K}\mathbf{x} = \mathbf{u} \tag{1}$$

with block diagonal mass matrix $\mathbf{M} = \mathrm{diag}(\mathbf{M}_1, \mathbf{M}_2, \ldots, \mathbf{M}_n)$ and stiffness matrix

DOI: 10.1002/stc

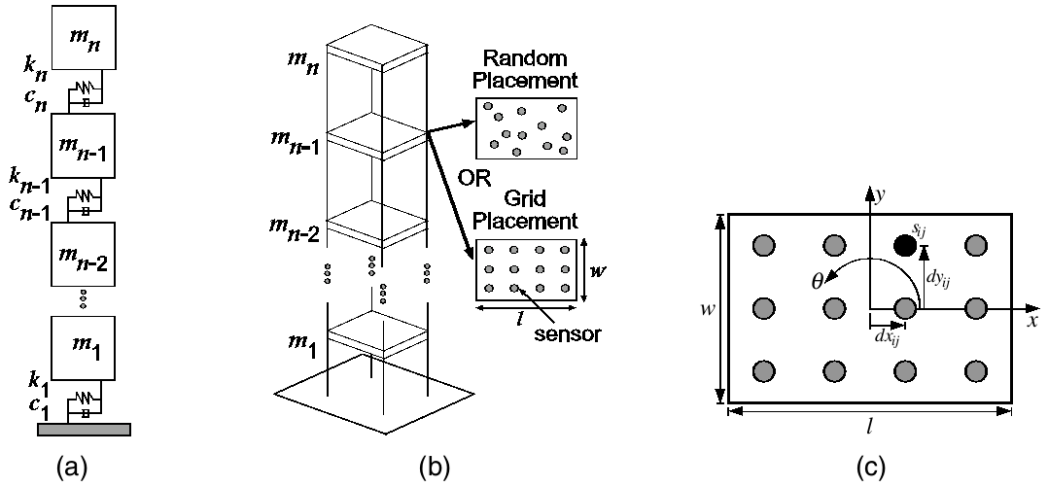

Figure 1. (a) Shear structure (showing one direction only). (b) An n-story structure with sensors placed randomly or in a grid on each floor. (c) Floor diagram with distances dx_{ij} and dy_{ij} from the center of the floor to sensor $\boldsymbol{s_{ij}}$.

$$\mathbf{K} = \begin{bmatrix} \mathbf{K}_1 + \mathbf{K}_2 & -\mathbf{K}_2 & 0 & \cdots & 0 \\ -\mathbf{K}_2 & \mathbf{K}_2 + \mathbf{K}_3 & \ddots & \ddots & \vdots \\ 0 & \ddots & \ddots & \ddots & 0 \\ \vdots & \ddots & \ddots & \mathbf{K}_{n-1} + \mathbf{K}_n & -\mathbf{K}_n \\ 0 & \cdots & 0 & -\mathbf{K}_n & \mathbf{K}_n \end{bmatrix}, \tag{2}$$

where $\mathbf{M}_i$ is the mass matrix of the ith floor, $\mathbf{K}_i$ is the stiffness matrix of the ith story, $\mathbf{x} = [x_1, y_1, \theta_1, \ldots, x_n, y_n, \theta_n]^T$ is the displacement/rotation vector relative to the ground, and $\mathbf{u}$ is the external force/moment vector. Damping matrix $\mathbf{C}$ is chosen such that the damping ratio of every mode is ζ (i.e., $\mathbf{C} = \mathbf{M}\Phi(2\zeta\Lambda^{1/2})\Phi^{-1}$ where Λ and Φ are the diagonal matrix of eigenvalues and corresponding matrix of eigenvectors found from $\mathbf{K}\Phi = \mathbf{M}\Phi\Lambda$). The structure in the numerical example herein is symmetric with $\mathbf{M}_i = \text{diag}[m, m, m_\theta]$ and $\mathbf{K}_i = \text{diag}[k_x, k_y, k_\theta]$ where $m_\theta = m(w^2 + l^2)/12$ and $k_\theta = (k_x w^2 + k_y l^2)/4$, with floor mass $m = 4.90$ kg (10.8 lb), story stiffnesses $k_x = 438$ kN/m (25000 lbs/in) and $k_y = 219$ kN/m (12 500 lbs/in), and damping ratio $\zeta = 5$ % in every mode.

Figure 2. Four-story building model used in Chintalapudi *et al*. [33].

DOI: 10.1002/stc

3.2. Effect of sensor placement on measurements

Let s_{ij} denote the jth sensor ($j = 1, 2, \ldots, m$) on the ith floor ($i = 1, 2, \ldots, n$), and let x_{ij} and y_{ij} be the measurements recorded by sensor s_{ij} in the x and y directions, respectively. In Figure 1(c), dx_{ij} and dy_{ij} are the distances from the center of the ith floor to sensor s_{ij}. The relationship between (x_{ij}, y_{ij}) and the ith floor's movements (x_i, y_i, θ_i) is given by

$$\begin{bmatrix} x_{ij} \\ y_{ij} \end{bmatrix} = \begin{bmatrix} 1 & 0 & -dy_{ij} \\ 0 & 1 & dx_{ij} \end{bmatrix} \begin{bmatrix} x_i \\ y_i \\ \theta_i \end{bmatrix}, \tag{3}$$

assuming θ_i is small and, thus, $\theta_i \approx \sin(\theta_i)$. Here, x_i and y_i are the displacements in the x and y directions, and θ_i is the rotation of the ith floor, all relative to the ground. For m sensors, Equation (3) can be expanded as

$$\begin{bmatrix} x_{i1} & y_{i1} & x_{i2} & y_{i2} & x_{im} & y_{im} \end{bmatrix}^T = \begin{bmatrix} 1 & 0 & 1 & 0 & \ldots & 1 & 0 \\ 0 & 1 & 0 & 1 & \ldots & 0 & 1 \\ -dy_{i1} & dx_{i1} & -dy_{i2} & dx_{i2} & \ldots & -dy_{im} & dx_{im} \end{bmatrix}^T \begin{bmatrix} x_i \\ y_i \\ \theta_i \end{bmatrix}, \tag{4}$$

or, in matrix notation, by

$$\mathbf{X}_{si} = \mathbf{Q}\mathbf{X}_i. \tag{5}$$

With pseudo-inverse $\mathbf{Q}^+ = (\mathbf{Q}^T\mathbf{Q})^{-1}\mathbf{Q}^T$, the floor movement can be estimated from the sensor measurements as

$$\mathbf{X}_i = \mathbf{Q}^+\mathbf{X}_{si}. \tag{6}$$

This is a least square estimate of floor movements, where the lateral movements x_i and y_i are affected by the accuracy of measurements, and the rotation θ_i additionally affected by the sensor locations (dx_{ij}, dy_{ij}). Large dx_{ij} and dy_{ij} are expected to improve the accuracy of the rotation estimates because sensors further away from the rotating axis (center of the floor) can better record the effects of rotations. This is because the movements due to θ_i are larger with large dx_{ij} and dy_{ij} as compared with that due to the same θ_i with small dx_{ij} and dy_{ij}. Because there is noise in sensor measurements, Equation (6) is more realistically represented as

$$\hat{\mathbf{X}}_i = \mathbf{Q}^+(\mathbf{X}_{si} + \mathbf{W}), \tag{7}$$

where $\mathbf{W}$ is a vector of measurement noise, which is assumed to be independent and normally distributed with zero-mean and variance p_{ij}, or $N(0, p_{ij})$.

3.3. Network model

In the network model, it is assumed that the nodes can adjust their power levels up to a maximum power level $P_{\max}$ giving a maximum transmission range $R_{\max}$. Two nodes are able to communicate with each other if the Euclidean distance between them is less than or equal to the minimum of their transmission ranges. This model, commonly known as the *disk graph model*, is idealistic and does not capture interference and the anisotropic nature of radio propagation [36]. The center of each floor also has a high powered node, called the *local sink*, which connects nodes in adjacent floors to exchange measurements. Thus, all nodes in a floor only send their measurements to their local sink. In the simulations, $R_{\max}$ is taken as 91.44 cm (36 in.), chosen so that, at maximum power, all nodes can talk directly to each other.

3.4. Energy model

A wireless SHM system once deployed is expected to be functional for months or even years depending on how often a diagnosis is performed. Because battery-powered nodes are limited in energy, a crucial aspect of designing wireless SHM systems is to minimize the energy consumption. Although such systems usually have a very high sampling rate and resolution and may require intense CPU usage, the power consumption by the radio module is orders of magnitude higher than sampling and computation [37,38]. For example, the Tmote Sky platform, which uses a Chipcon CC2420 radio [40] operating at

DOI: 10.1002/stc

2.4 GHz using an IEEE 802.15.4 MAC/PHY layer, the currents drawn for transmission and reception are 17.4 and 19.7 mA, respectively. As these nodes use two AA batteries, supplying about 3.6 V, the resulting transmit and receive powers are 62 and 70 mW, respectively. For the sampling module, Tmote Sky uses an ultra-low power 8 MHz Texas Instrument MSP430 processor [41], which draws 1.8 mA when on, 0.054 mA when idle, and 0.0051 mA when on standby; the corresponding power consumptions are 6.4, 0.19, and 0.018 mW, respectively. Clearly, there are a number of factors that affect the durations of sampling and radio transmission/reception; in the studies herein, the durations were of comparable magnitude, making transmission/reception more costly than sampling.

Although various radios have different characteristics, a common feature is that the sleep mode generally consumes three orders of magnitude less power than transmission, reception, or idle modes. Thus, to cut down on the energy costs, it is best to keep the radio in the sleep mode for as long as possible and to transmit packets at a high data rate so as to minimize the transmission time. In this paper, the following energy model is considered where the energy expenditure per bit for communication over a link of length d is

$$e(d) = \alpha + \beta(d/w)^{\eta}, \tag{8}$$

where the distance-independent term α represents the energy cost of transmitter and receiver electronics with a typical value between 70 and 100 mW for 2.4 GHz radios; β/w^{η} is the transmit amplifier constant, which is normalized by the width w of the structure; and η is the path-loss exponent with typical values between 2 and 6 depending on the environment. Here, d^{η} captures the amplification required to ensure constant power reception at the receiver. In the simulations herein, $\alpha = 70$ mW, $\beta = 6144$ mW, and $\eta = 4$.

4. SYSTEM IDENTIFICATION USING EIGENSYSTEM REALIZATION ALGORITHM

Using measurements from the sensors, the structural characteristics can be identified by first estimating the modal parameters such as frequencies and mode shapes with the ERA. The ERA was originally developed by Juang and Pappa [39] and is a well-known scheme for estimating state-space realizations of a system from impulse responses. It uses a singular value decomposition of the following Hankel matrix:

$$\mathbf{H}(k-1) = \begin{bmatrix} \mathbf{Y}(k) & \mathbf{Y}(k+1) & \dots & \mathbf{Y}(k+p) \\ \mathbf{Y}(k+1) & \mathbf{Y}(k+2) & \dots & \mathbf{Y}(k+p+1) \\ \vdots & \vdots & \ddots & \vdots \\ \mathbf{Y}(k+r) & \mathbf{Y}(k+r+1) & \dots & \mathbf{Y}(k+p+r) \end{bmatrix}, \tag{9}$$

where $\mathbf{Y}(k)$ is the $m \times b$ pulse matrix such that $Y_{ij}(k)$ is the impulse response at the kth time instant collected at the ith location due to an impulsive excitation at the jth location in the structure. The singular value decomposition of $\mathbf{H}(0)$ is given by

$$\mathbf{H}(0) = \mathbf{P}\mathbf{D}\mathbf{Q}^T, \tag{10}$$

where $\mathbf{P}$ and $\mathbf{Q}^T$ are unitary matrices formed by left and right singular vectors, respectively, and $\mathbf{D}$ is the diagonal matrix formed by the singular values. Singular vectors corresponding to small singular values are attributed to noise, and the reduced order matrices $\mathbf{P}_n$, $\mathbf{Q}_n$ and $\mathbf{D}_n$ are generated by using only the singular vectors corresponding to the large singular values. The linear system parameters corresponding to the reduced order system can now be estimated using the equations:

$$\mathbf{A} = \mathbf{D}_n^{-1/2}\mathbf{P}_n^T\mathbf{H}(1)\mathbf{Q}_n\mathbf{D}_n^{-1/2} \tag{11}$$

$$\mathbf{B} = \mathbf{D}_n^{-1/2}\mathbf{Q}_n^T\mathbf{E}_b \tag{12}$$

$$\mathbf{C} = \mathbf{E}_m^T\mathbf{P}_n\mathbf{D}_n^{-1/2} \tag{13}$$

where $\mathbf{E}_i^T = [\mathbf{I}_i \ 0]$ with $\mathbf{I}_i$ being the identity matrix of order i. The mode shapes of the structure correspond to the columns in the matrix $\mathbf{V} = \mathbf{C}\ \Phi$, where Φ contains the eigenvectors of $\mathbf{A}$; the modal frequencies of the structure correspond to the magnitude of the eigenvalues of $\mathbf{A}$.

DOI: 10.1002/stc

To check the accuracy of the system identification using various sensor placements, comparisons are made between mode shapes estimated using the ERA from measured responses with and without noises. The noise-free estimated mode shapes are used as the baseline case with which other estimated mode shapes (with different noise levels) are compared. Because mode shapes, similar to eigenvectors, are scalable vectors for specific frequencies, the *modal amplitude coherence* (MAC) is used to differentiate between different sets of mode shapes [39]. The MAC between two vectors **a** and **b** is defined as

$$\mathrm{MAC}(\mathbf{a},\mathbf{b}) = \frac{|\mathbf{a}^*\cdot\mathbf{b}|}{\sqrt{(\mathbf{a}^*\cdot\mathbf{a})(\mathbf{b}^*\cdot\mathbf{b})}} \tag{14}$$

with values ranging from 0 to 1, where $\mathbf{a}^*$ denotes complex conjugate of **a**. When two vectors are parallel, their MAC value is 1, whereas two orthogonal vectors have a MAC value of 0. Thus, by finding the MAC values of the mode shapes from the base case and from cases with different sensor placements and noise levels, accuracy can be measured. For square matrices $\mathbf{A} = [\mathbf{a}_1, \mathbf{a}_2, \ldots, \mathbf{a}_k]$ and $\mathbf{B} = [\mathbf{b}_1, \mathbf{b}_2, \ldots, \mathbf{b}_k]$, the MAC is defined as

$$\mathrm{MAC}(\mathbf{A},\mathbf{B}) = \begin{bmatrix} \mathrm{MAC}(\mathbf{a}_1,\mathbf{b}_1) & \mathrm{MAC}(\mathbf{a}_1,\mathbf{b}_2) & \ldots & \mathrm{MAC}(\mathbf{a}_1,\mathbf{b}_k) \\ \mathrm{MAC}(\mathbf{a}_2,\mathbf{b}_1) & \mathrm{MAC}(\mathbf{a}_2,\mathbf{b}_2) & \ldots & \mathrm{MAC}(\mathbf{a}_2,\mathbf{b}_k) \\ \vdots & \vdots & \ddots & \vdots \\ \mathrm{MAC}(\mathbf{a}_k,\mathbf{b}_1) & \mathrm{MAC}(\mathbf{a}_k,\mathbf{b}_2) & \ldots & \mathrm{MAC}(\mathbf{a}_k,\mathbf{b}_k) \end{bmatrix}, \tag{15}$$

Error is measured as the Frobenius norm of $\left(\mathrm{MAC}\left(\hat{\Phi},\Phi\right) - \mathbf{I}\right)$ or

$$error = \sqrt{trace\left(\left[\mathrm{MAC}\left(\hat{\Phi},\Phi\right) - \mathbf{I}\right]^T\left[\mathrm{MAC}\left(\hat{\Phi},\Phi\right) - \mathbf{I}\right]\right)}, \tag{16}$$

where $\hat{\Phi}$ is the estimated mode shape from the measured responses of the structure and **I** is the identity matrix. When $\hat{\Phi} = \Phi$, $\mathrm{MAC}\left(\hat{\Phi},\Phi\right) = \mathbf{I}$ and $error = 0$.

5. MODE SHAPE ERRORS FROM SIMULATIONS

Two types of node deployments are studied: random and grid. In random deployment, nodes are placed randomly on each floor with uniform distributions in both x and y directions. The number of sensors per floor m and the noise level p are varied to study their effects on the mode shape error. For a given floor, 1000 realizations of random sensor placement are simulated and analyzed for different noise levels. In grid deployment, nodes are placed on all floors with different inter-node separations. As before, the number of sensors per floor and the noise levels are varied to study their effects.

Using a structural model with four floors described in Figure 2, there are 12 modes (four floors each with three degrees of freedom x, y, and θ) in this structure. Model parameters are estimated using ERA with the structure being simulated with impulses (i.e., 24 singular values or 12 modes are found with ERA analysis). However, not all 12 real modes can be successfully identified. There are usually a few unidentifiable modes because of noise in the data, which have unpredictable effect on the mode shape error. To deal with the noise modes, the authors choose to include only five modes for the rest of the study (shown in the Table I), which are always identified from all the simulation cases. The authors acknowledge that relying only on the five modes can sometimes favor sensor placements with poor performance. For example, a placement that can successfully identify eight modes should be viewed more superior than another placement that only identifies five modes. In other words, the number of successfully identified modes should also be factored in measuring the SHM performance. However, for simplicity, only these five reliable modes are considered.

Table I. Total of 12 modes out of which only five are reliable (shown in bold).

Mode	1	2	3	4	5	6	7	8	9	10	11	12
Frequency (Hz)	**2.51**	**3.55**	**4.97**	**7.22**	**10.21**	11.06	13.57	14.30	15.64	19.19	21.91	26.87

DOI: 10.1002/stc

5.1. Random deployment

In random deployment, the sensors are uniformly distributed on each floor. In other words, dx_{ij} and dy_{ij} have uniform and independent distributions of $U(-l/2, l/2)$ and $U(-w/2, w/2)$, respectively. A random deployment might not be the best placement strategy with respect to the accuracy of measurements and network connectivity, but it facilitates looking at a wide range of different deployment configurations. Figure 3 shows the mode shape errors of 1000 realizations simulated for different combinations of the number of sensors per floor ($m = 2, 3, \ldots, 10$) and noise levels ($p = 2\,\%, 4\,\%, \ldots, 10\,\%$) relative to the maximum response. Clearly, as p increases, so do the errors. Meanwhile, increasing m lowers the overall errors because more sensors can improve measurements averaging out the assumed white sensor noise. Typically, the mode shape errors converge to a single band as m increases, but for some noise levels ($p = 8\,\%, 10\,\%$) the errors converge into two bands.

To understand the relationship between sensor deployment and mode shape errors, the realizations with the best and worst errors are further examined. For $m = 3$ sensors and $p = 8\,\%$ noise level, comparing five different cases with highest and lowest errors, it is observed that the sensors in the low error cases are less clustered than those in the high error cases. This observation falls in line with the mathematical interpretation that the accuracy of rotation estimate increases as the distance between the sensors increases. For realizations with a larger number of sensors per floor ($m = 7$) and the same noise level ($p = 8\,\%$), there is no significant difference in clustering between the high and low error cases; as a result, no conclusive inference could be drawn from the observations for these cases.

5.2. Grid deployment

In grid deployment, for a given number m of sensors per floor, $m = m_1 \times m_2$ grids are formed with different inter-node separations, and one sensor is placed at each grid point. To maintain connectivity on each floor, the maximum inter-node separation is assumed to be smaller than the communication range of a node. The objective here is to study the relationship among the number of sensors deployed, their inter-node separations, and the mode shape error for a given floor dimension.

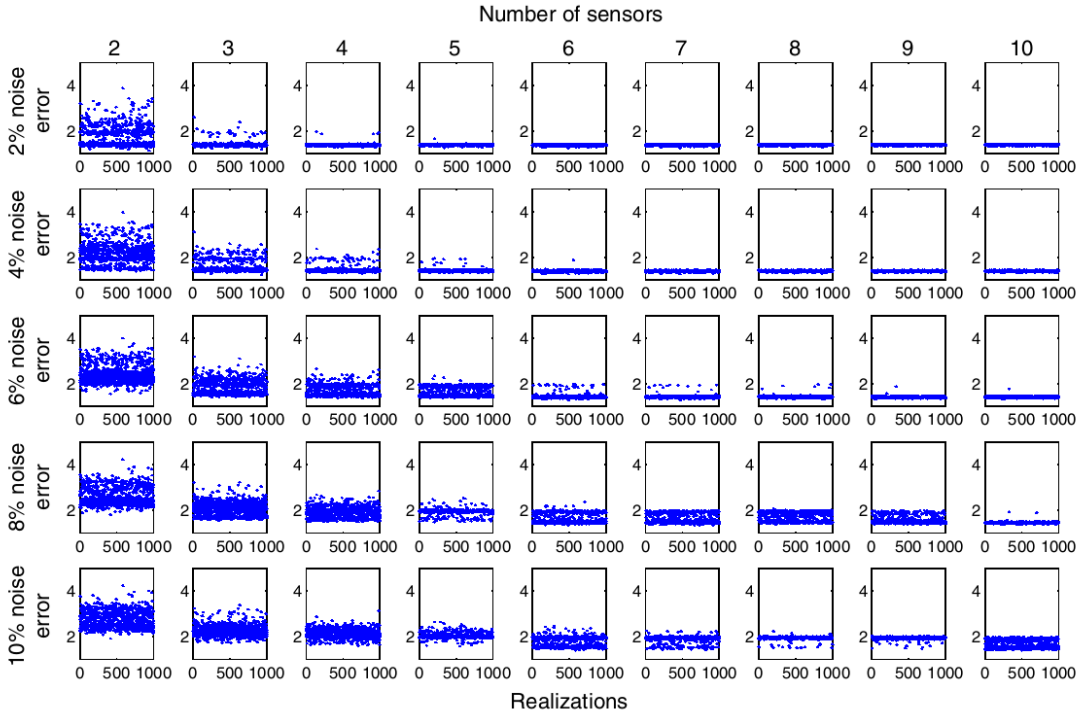

Figure 3. Mode shape errors of 1000 realizations with different numbers of sensors and noise levels. The errors in some cases converge into a single band and in other cases into two bands.

DOI: 10.1002/stc

Figure 4(b) illustrates the corresponding mode shape error for each of the configurations shown in Figure 4(a), which decreases sharply as the nodes are placed further apart from each other. However, after a certain point, when the separation reaches around $0.15w$ (where w is the width of the floor), the rate of decrease flattens out. A similar trend is observed when the number of sensors per floor is increased keeping the noise level fixed at 4 %. These results indicate the expected observation that a large number of sensors when placed further apart reduce the mode shape errors, although with diminishing returns.

6. ACCURACY AND ENERGY EFFICIENCY

The results presented in the previous section show that the mode shape error decreases with increasing inter-node separation and the number of sensors per floor, although with diminishing returns. However, as the separation increases, a node must transmit at a higher power level to reach its neighbors, which requires more energy. Similarly, a large number of sensors also results in high energy consumption. The goal in this section is to study this trade-off and find an optimal grid separation and number of sensors per floor to balance minimizing the amount of energy consumed in communicating the measurements with minimal error in mode shape estimation. On the basis of the network model described in Section 3.3, an energy efficient routing tree is first constructed assuming that all the nodes on a given floor can send their measurements to a local sink located at the center of that floor. Then, from the energy model described in Section 3.4, the total energy spent for gathering all the measurements over the routing tree to the local sink is estimated for a given inter-node separation. Finally, simulations show the trends in energy consumption with varying inter-node separation and the number of nodes.

6.1. Energy-balanced routing tree

Consider the scenario in which data measured by a set of m nodes on each floor must be delivered to the local sink located at the center of that floor. According to the energy model herein, the energy dissipation at a sensor node is proportional to the total number of bits the node receives and transmits. To increase the longevity of the network, a fair utilization of energy resources is needed so that no node suffers from an early energy depletion. Thus, it is important to construct an energy-balanced routing tree that will ensure uniform energy dissipation among all nodes. Assuming there is no data aggregation *en route* to the sink, the number of bits received by a node, and hence the energy required to transmit them, is proportional to the size of its sub-tree.

Let $e(T, i)$ be the energy spent by node i to send its measurements to the local sink over a routing tree T that is rooted at the sink. Assume that each node generates k bits of data. The goal is to construct an energy-balanced routing tree such that the following condition holds: (i) total energy spent by all the m nodes is minimized, and (ii) maximum energy spent by any node is minimized.

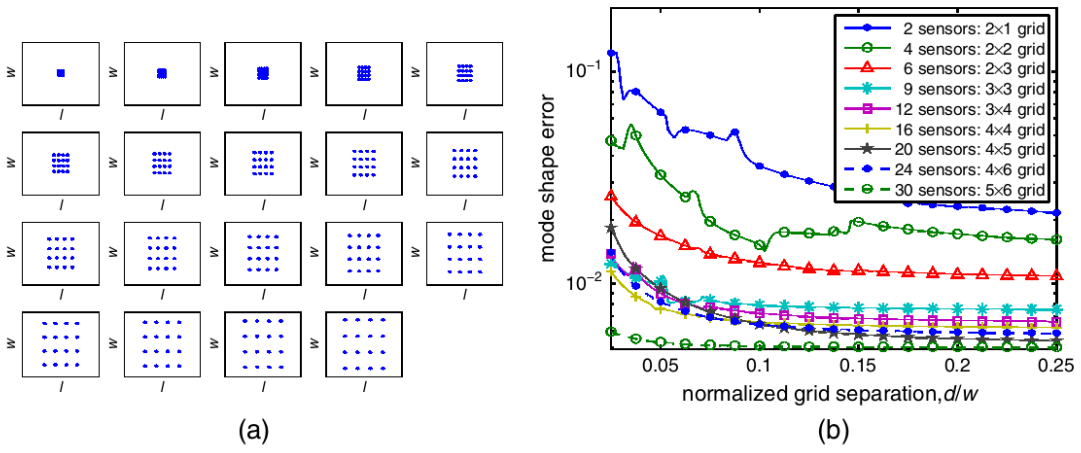

Figure 4. (a) Nineteen different configurations in grid deployment. (b) Effect of the number of sensors and distances on mode shape error with 4% noise level.

DOI: 10.1002/stc

It is assumed that the nodes can organize themselves into levels on the basis of their hop distance from the sink, with lower levels corresponding to nodes that are closer to the sink, as illustrated through an example in Figure 5(a). For a distance-dependent energy model, the first condition corresponds to a shortest path routing tree in terms of hop distance, where each node other than the sink selects one of its nearest neighbors from the previous level as its parent. Note that in a grid deployment, all nodes except those at the first level have two choices as their nearest neighbors from their previous levels. The best choice is made in such a way that the resulting sizes of the sub-trees rooted at the nearest neighbors are as close to each other as possible. This will ensure that the size of a sub-tree rooted at a lower level node is at least equal to or greater than that at a higher level node. At each level, this parent assignment strategy could be achieved either in a centralized or distributed way by exchanging messages between the neighboring nodes.

Note this particular parent assignment strategy may not always guarantee a min–max fair, energy-balanced routing tree on an arbitrary deployment of nodes where each node generates possibly a different amount of data (e.g., if one node has a single accelerometer and another has a triaxial accelerometer). However, for a grid deployment where each node generates the same amount of data (k bits), choosing the *best* nearest neighbor from the previous level will result in a min–max fair, energy-balanced tree. This is because choosing a neighbor from the previous level that is not one of the nearest ones will require more energy and, therefore, violate the first condition. Moreover, this will not help in better energy balancing because the amount of data generated by all the nodes is the same and the sink is located at the center of the floor.

It should be noted that instead of constructing a tree in which every node has a single parent, one could employ a non-tree-based or graph-based routing strategy, wherein a single node can have more than one parent. In such cases, for example, the uppermost node on the right at level 4 in Figure 5(a) can use both of the nodes at level 3, one to its left and one below, for sending its data in order to load balance energy consumption. However, typically in a sensor network, the nodes are organized as a tree, which makes routing simpler and easier to maintain; this assumption is made herein.

6.2. Energy consumption per floor

Having constructed a min–max fair, energy-balanced routing tree for a grid deployment, an expression is derived in this section for the total amount of energy required to route all data on a floor to a local sink, located at the center of the floor, as a function of grid separation.

As before, the grid deployment for each floor has $m_1 \times m_2$ sensors with grid separation d. The routing tree constructed on such a configuration is symmetric around the sink node, that is, the sub-trees rooted at the level 1 nodes are identical. The number γ of level 1 nodes depends on the values of m_1 and m_2. For m_1 and m_2 both odd (Figure 5(a)) or both even (Figure 5(b)), there are four level 1 nodes (i.e., $\gamma = 4$), and the

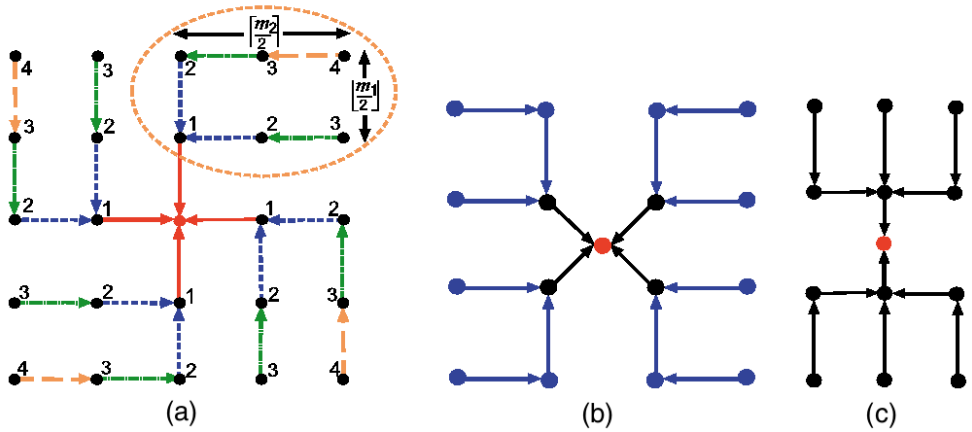

Figure 5. Min–max fair, energy-balanced routing trees on grid deployment: (a) numbers indicate levels; arrows correspond to routing paths from nodes at different levels; sink is on a grid point. (b) Four level 1 nodes with the sink at the center of a grid cell. (c) Two level 1 nodes with the sink at the center of a grid line.

DOI: 10.1002/stc

sink is located either on a grid point or at the center of a grid cell. When one of m_1 and m_2 is odd and the other is even, there are only two level 1 nodes ($\gamma = 2$), and the sink is located at the center of a grid line (Figure 5(c)). Because the sub-trees rooted at the level 1 nodes are identical, their energy consumption to route all data to their respective level 1 nodes are the same. In the following, expressions are derived for the total energy consumption per floor to deliver all the bits generated by the sensors to the local sink located at the center of the floor.

Without loss of generality, consider the sub-tree rooted at the level 1 node just above the sink, as shown in dotted ellipse in Figure 5(a). The number of rows and columns in this sub-tree is $\lfloor m_1/2 \rfloor$ and $\lceil m_2/2 \rceil$, respectively, where $\lfloor \cdot \rfloor$ and $\lceil \cdot \rceil$ denote the floor and the ceiling integer of their argument. Because a node transmits its own data along with all data received from its own sub-tree, the total number of bits transmitted over a one-hop distance by all nodes in a given row to reach the leftmost node is

$$N_1 = k\left(\sum_{i=1}^{\lceil m_2/2 \rceil - 1} i\right) = \frac{k}{2}\lceil m_2/2 \rceil (\lceil m_2/2 \rceil - 1). \tag{17}$$

By symmetry, all rows transmit the same amount of data to reach their respective leftmost nodes. Therefore, the total number of bits transmitted over one hop to the leftmost nodes is $N_1 \lfloor m_1/2 \rfloor$. Finally, all data from the leftmost nodes at each row are transmitted to the level 1 node. Thus, total bits transmitted by these leftmost nodes over a one-hop distance are

$$N_2 = k\lceil m_2/2 \rceil \left(\sum_{i=1}^{\lfloor m_1/2 \rfloor - 1} i\right) = \frac{k}{2}\lfloor m_1/2 \rfloor \lceil m_2/2 \rceil (\lfloor m_1/2 \rfloor - 1). \tag{18}$$

Finally, the level 1 node transmits all these data to the sink. Therefore, the total energy spent by all the nodes to get their data to the sink is given by

$$E(d) = \gamma(N_1 \lfloor m_1/2 \rfloor + N_2 + \lfloor m_1/2 \rfloor \lceil m_2/2 \rceil k) e(d). \tag{19}$$

Substituting Equations (17) and (18) into Equation (19) and simplifying yields:

$$E(d) = \frac{\gamma k}{2}\lfloor m_1/2 \rfloor \lceil m_2/2 \rceil (\lfloor m_1/2 \rfloor + \lceil m_2/2 \rceil) e(d), \quad \gamma = 4. \tag{20}$$

Following a similar procedure, the total energy spent to deliver all of the bits to the local sink when m_1 and m_2 are both even is

$$E(d) = \frac{\gamma k}{2}\lfloor m_1/2 \rfloor \lceil m_2/2 \rceil \left(\lfloor m_1/2 \rfloor + \lceil m_2/2 \rceil + \sqrt{2} - 2\right) e(d), \quad \gamma = 4, \tag{21}$$

and, when m_1 is odd and m_2 is even, is

$$E(d) = \frac{\gamma k}{2}\lceil m_2/2 \rceil \left(m_1 \lceil m_2/2 \rceil + 2\lfloor m_1/2 \rfloor^2 + 2\lfloor m_1/2 \rfloor\right) e(d), \quad \gamma = 2. \tag{22}$$

Note that when m_1 is even and m_2 is odd, one can always rotate the view point and take m_1 as odd and m_2 as even and Equation (22) will apply.

6.3. Location and number of sensors

The simulation results presented so far indicate that the mode shape error decreases with increasing inter-node separation and the number of nodes. However, an increase in the number of nodes leads to the generation of more data, and an increase in inter-node separation requires higher transmission power. The combination of these two effects, consequently, results in an increase in energy consumption. Thus, these two opposing factors lead to a joint optimization problem of finding the right grid separation and the number of nodes that will optimally balance the mode shape errors with energy consumption. For ease of presentation and understanding, the optimization is first illustrated through an example with fixed number of nodes for finding the optimal grid separation and energy consumption and then extended to incorporate optimality on the number of nodes.

In Figure 6(a), the mode shape errors and the energy consumption per floor with increasing grid separations are plotted for 16-node configurations. The mode shape errors are high at small grid separations, whereas the energy consumption is high at large grid separations. Denoting the mode shape error

DOI: 10.1002/stc

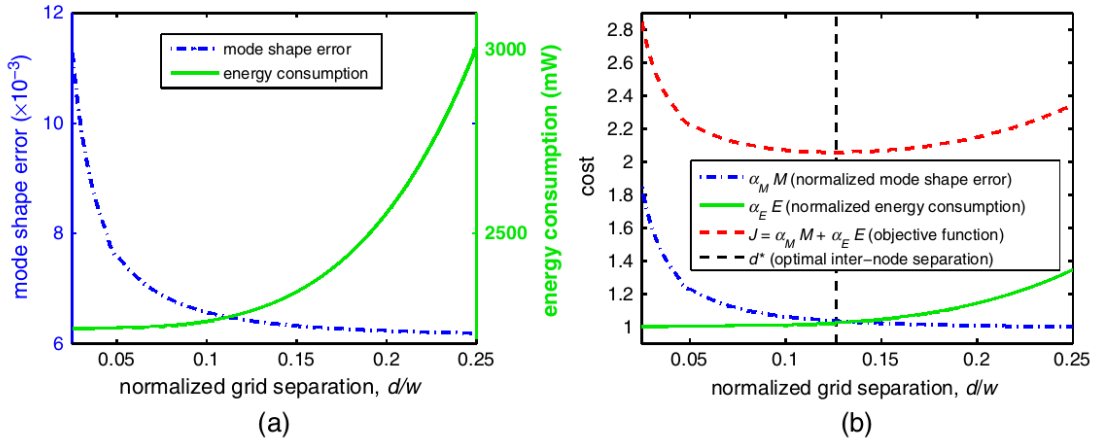

Figure 6. Comparison of mode shape error and energy consumption for different grid separations.

by $M(d)$ and the energy consumption per floor by $E(d)$ at separation d, the optimal separation d^* can be found by minimizing the following objective function:

$$J = \alpha_M M(d) + \alpha_E E(d), \qquad d_{\min} \leqslant d \leqslant d_{\max} \tag{23}$$

where α_M and α_E are weighting constants. The choice of α_M and α_E heavily depends on the relative cost of the mode shape error and the energy consumption. The optimal d^* is bounded by the minimum and maximum allowable separations, $d_{\min}$ and $d_{\max}$, respectively, which are influenced by the sensor configurations. Figure 6(b) illustrates the objective function of Equation (23) using the following values for α_M and α_E:

$$\alpha_M = 1/\min_d M(d) \qquad \text{and} \qquad \alpha_E = 1/\min_d E(d). \tag{24}$$

Here, although $\min_d M(d)$ and $\min_d E(d)$ are the minimum values over $d \in [d_{\min}, d_{\max}]$, they approximate the absolute minimum values without constraining d because the range $[d_{\min}, d_{\max}]$ is sufficiently wide. For the 16-node configuration, $M(d)$ and $E(d)$ asymptotically approach their absolute minimum values. The numerical solution for d^*, as shown in Figure 6(b), is approximately $0.1265w$. The constants α_M and α_E in Equation (24) are used to normalize $M(d)$ and $E(d)$ such that they are equally weighted in optimizing d.

Extending to jointly optimize the grid separation and the number of nodes, the cost (23) becomes

$$J = \alpha_M M(d, m) + \alpha_E E(d, m). \tag{25}$$

where $M(d, m)$ and $E(d, m)$ are the mode shape error and energy consumption, respectively, for m sensors per floor at grid separation d. As before, the weighting constants can be expressed as

$$\alpha_M = 1/\min_{d,m} M(d, m) \qquad \text{and} \qquad \alpha_E = 1/\min_{d,m} E(d, m). \tag{26}$$

Minimizing (25) over d and m gives d^* and m^* such that moving away from (d^*, m^*) will result in no improvement in the mode shape error or energy consumption that will not be outweighed by the decrease in the other measure. Figure 7(a) and (b) shows how $M(d, m)$ and $E(d, m)$ change with respect to both the grid separation and the number of sensors per floor (among the set of nine possible grid deployments given in Figure 4(b), respectively). Figure 7(c) illustrates the objective function (25) with α_M and α_E from (26). The optimal pair of values are $(d^* = 0.1025w, m^* = 4)$ in this particular example.

The weights in (23) and (25) are used to accommodate with different units and scales of the mode shape error and the energy consumption. The relative importance of the mode shape error and the energy consumption can be varied by adjusting the weights α_M and α_E, which in turn will affect the optimal solutions for d^* and/or m^*, favoring either the accuracy in mode shape estimation or the energy efficiency. For example, decreasing α_M while keeping α_E unchanged will lessen the weight on the mode shape estimation relative to the energy efficiency in the optimization and vice versa.

Figure 8 demonstrates the effect of different values of α_M and α_E on the optimal solutions for d^* in minimizing (23). In Figure 8(a) and (b), instead of using (24), α_M and α_E are set to different values such

DOI: 10.1002/stc

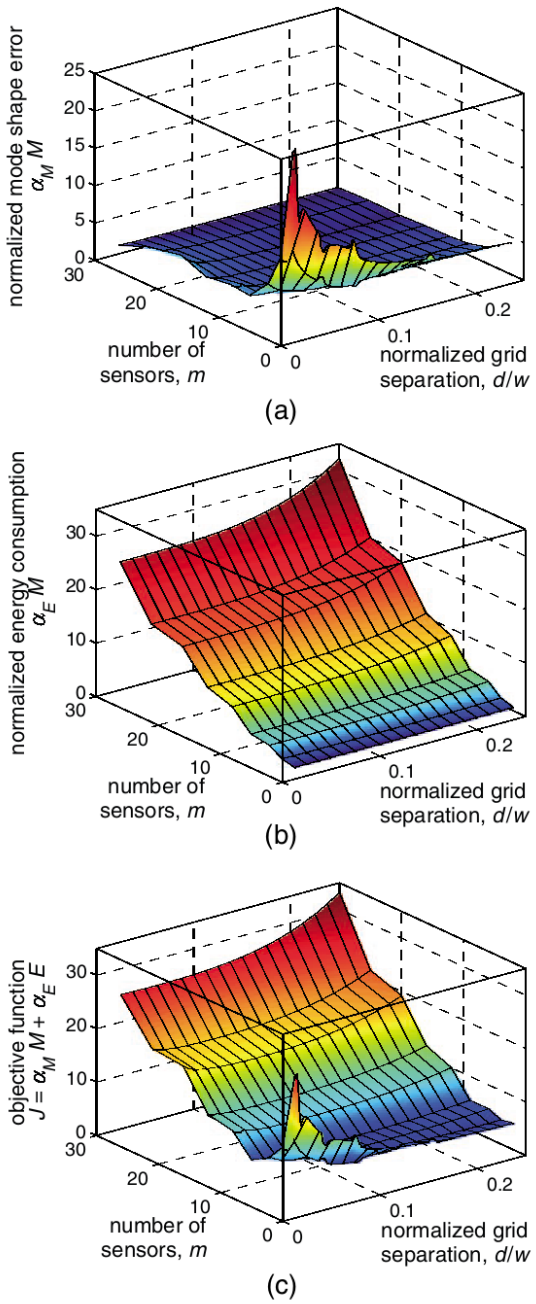

Figure 7. (a) Normalized mode shape error $\alpha_M M$, (b) normalized energy consumption $\alpha_E E$, and (c) objective function $J = \alpha_M M + \alpha_E E$, all as functions of the number of sensors and grid separation.

that more weight is given to energy efficiency. The optimal grid separation d^* is now $0.1198w$ instead of $0.1265w$. The decreased d^* improves energy usage by reducing the radio transmission range. In contrast, more weight is given to the mode shape estimation in Figure 8(c) and (d); the optimal separation increases to $0.1299w$. Depending on the relative cost of the mode shape estimation and the energy consumption, different values of α_M and α_E should be given to the objective functions in (23) and (25).

The results shown herein are, of course, based on a shear structure with simple rectangular floor layouts and a particular method for estimating mode shapes. Different floors layouts and types of structures (e.g., bridges, trusses) may lead to different preferred placements of sensors and sinks (data receivers). For example, bridges may have the largest displacement in the middle of spans but may have sinks at the ends of the bridges or at tower locations. This is quite a different topology than the

DOI: 10.1002/stc

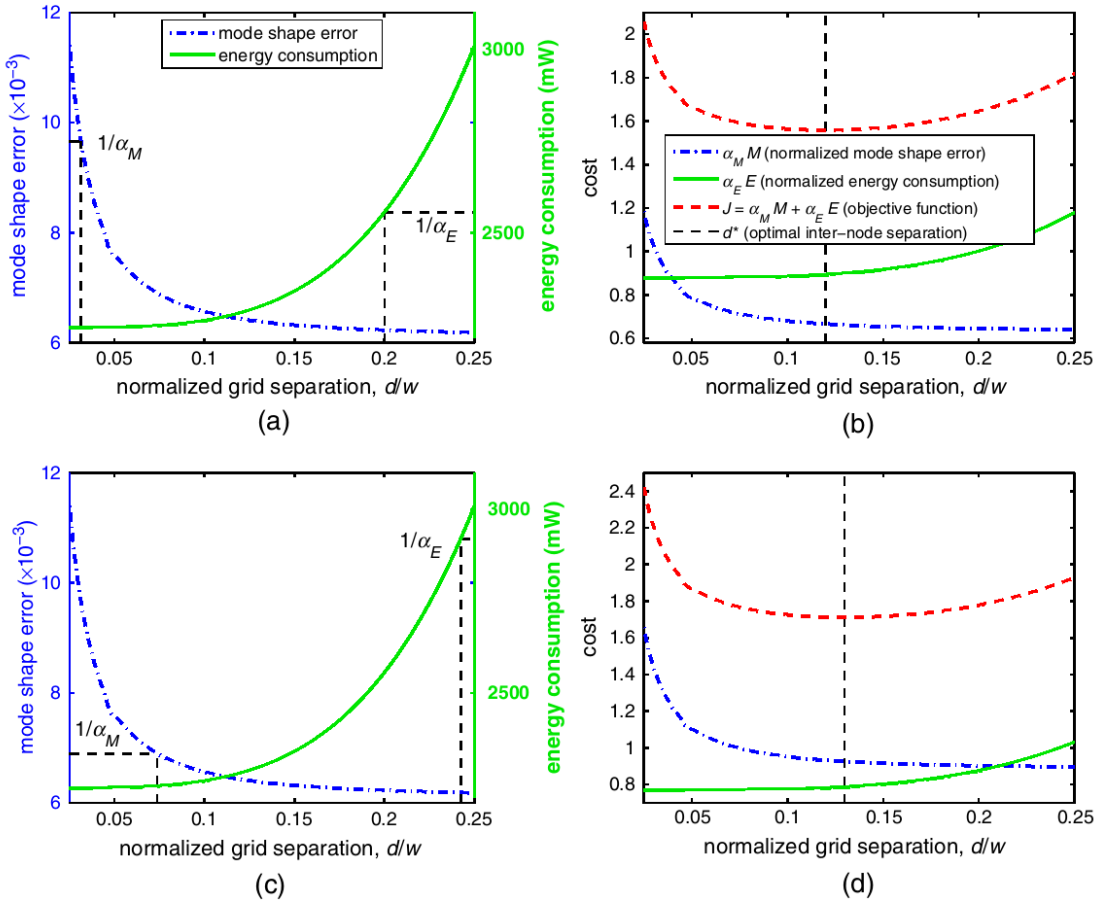

Figure 8. (a) Mode shape error and energy consumption with more weight given to energy efficiency. (b) The corresponding objective function value for (a). (c). Mode shape error and energy consumption with more weight given to mode shape estimation. (d) The corresponding objective function for (c).

problem studied herein. However, the trade-offs between energy efficiency and SHM accuracy are similar, and the proposed methodology could be easily applied to other types of structures. Similarly, the ERA for mode shape estimation could be replaced with other identification approaches in the time or frequency domains. The particular results may change, such as the exact optimal separation distances, but there will always remain a trade-off between accuracy and energy consumption; sensors located where the effective signal-to-noise ratio is strong are often not the locations for minimal power.

7. CONCLUSIONS AND FUTURE WORK

Wireless SHM systems are promising due to their ease of installation, inexpensive costs, and scalability. However, a WSN comes with its power and bandwidth constraints. This paper provides a study on optimizing sensors placements for SHM in terms of the quality of system identification and energy cost. These two opposing metrics prefer a tight placement of a few sensors to decrease the energy cost and a separated placement of many sensors to increase the accuracy in estimating structural modal parameters. A compromise is suggested by defining an objective function with weighting factors on energy needs and estimation accuracy. The number of sensors and the distances between them are analyzed using the multivariate objective function and an optimal sensor separation is found. The effect of an optimal placement due to different weights is also analyzed. Future work will involve optimal deployment for more complex structures in terms of floor layouts, non-shear structures, sensor failures, realistic wireless interference models, data transfer time efficiency, and so on. Experiments in a laboratory setting are needed to further validate the result of this study. Furthermore, an existing building is suitable for future

DOI: 10.1002/stc

investigation where practical difficulties in deploying sensors, real world noise, movements in the building, and factors affecting the quality of system identification cannot be foreseen in simulation.

ACKNOWLEDGEMENTS

The first and third authors gratefully acknowledge the partial support by the National Science Foundation under CAREER award CMS 00-94030 and through grants ANI 03-25875 and CMMI 08-26634. The second and fourth authors gratefully acknowledge the partial support by the National Science Foundation under grant CNS 03-47621. Any opinions, findings, and conclusion or recommendations expressed herein are those of the authors and do not necessarily reflect the views of the National Science Foundation.

REFERENCES

1. Lynch JP, Loh KJ. A summary review of wireless sensors and sensor networks for structural health monitoring. *The Shock and Vibration Digest* 2006; **38**(2):91–128.
2. Straser EG, Kiremidjian AS. A modular wireless damage monitoring system. *Technical Report*, Department of Civil and Environmental Engineering, Stanford University, Stanford, CA, 1998.
3. Gao Y, Spencer BF Jr, Ruiz-Sandoval M. Distributed computing strategy for structural health monitoring. *Structural Control and Health Monitoring* 2006; **13**(1):488–507.
4. Sodano HA, Inman DJ, Park G. A review of power harvesting from vibration using piezoelectric materials. *Shock and Vibration Digest* 2004; **36**(3):197–205.
5. Wang L, Yuan FG. Energy harvesting by magnetostrictive material (MsM) for powering wireless sensors in SHM. *Smart Structures and Materials & NDE and Health Monitoring*, 2007; 18–22.
6. Paek J, Chintalapudi KK, Govindan R, Caffrey J, Masri S. A wireless sensor network for structural health monitoring: performance and evaluation. *EmNetS*, Sydney, Australia, 2005; 1–10.
7. Xu N, Rangwala S, Chintalapudi KK, Ganesan D, Board A, Govindan R, Estrin D. A wireless sensor network for structural monitoring. *ACM SenSys*, Baltimore, MD, 2004; 13–24.
8. Kurata N, Spencer BF Jr, Ruiz-Sandoval M. Risk monitoring of buildings with wireless sensor networks. *Structural Control and Health Monitoring* 2005; **12**:315–327.
9. Ni YQ, Xia Y, Liao WY, Ko JM. Technology innovation in developing the structural health monitoring system for Guangzhou new TV tower. *Structural Control and Health Monitoring* 2009; **16**(1):73–98.
10. Jang S, Jo H, Cho S, Mechitov KA, Rice JA, Sim SH, Jung HJ, Yun CB, Spencer BF Jr, Agha GA. Structural health monitoring of a cable-stayed bridge using smart sensor technology: deployment and evaluation. *Smart Structures and Systems* 2010; **6**(5–6):439–459.
11. Kurata M, Kim J, Zhang Y, Lynch JP, van der Linden GW, Jacob V, Thometz E, Hipley P, Sheng LH. Long-term assessment of an autonomous wireless structural health monitoring system at the new Carquinez suspension bridge. *Proceedings of SPIE, the International Society for Optical Engineering* Vol. **7983**(2), San Diego, California, USA, March 7–10, 2011.
12. Spencer Jr BF, Cho SJ. Recent advances in wireless structural health monitoring of civil infrastructure. *Proceedings of International Symposium on Innovation & Sustainability of Structures in Civil Engineering*, Xiamen University, China, 28–30 October 2011.
13. Low CP. An approximation algorithm for the load balanced semi-matching problem in weighted bipartite graphs. *Information Processing Letters* 2006; **100**(4):154–161.
14. Huang SC, Jan RH. Energy-aware, load balanced routing schemes for sensor networks. *10th International Conference on the Parallel and Distributed Systems*, Newport Beach, CA, 7–9 July 2004; 419–425.
15. Gao J, Zhang L. Load-balanced short-path routing in wireless networks. *IEEE Transactions on Parallel and Distributed Systems* 2006; **17**(4):377–388.
16. Sim SH, Spencer BF Jr, Zhang M, Xie H. Automated decentralized modal analysis using smart sensors. *Structural Control and Health Monitoring* 2010; **17**:872–894.
17. Nagayama T, Spencer BF Jr, Rice JA. Autonomous decentralized structural health monitoring using smart sensors. *Structural Control and Health Monitoring* 2011; **16**:842–859.
18. Shah RC, Rabaey JM. Energy aware routing for low energy ad hoc sensor networks. *IEEE WCNC*, Orlando, FL, 2002; 350–355.
19. Dai H., Han R. A node-centric load balancing algorithm for wireless sensor networks. *IEEE Globecom*, San Francisco, CA, 2003; 548–552.
20. Chatterjee P, Das N. A distributed algorithm for load-balanced routing in multihop wireless sensor networks. *ICDCN*, Kolkata, India 2008; 332–338.
21. Casciati S, Chen ZC. A multi-channel wireless connection system for structural health monitoring applications. *Structural Control and Health Monitoring* 2010; **18**(5):588–600.
22. Nagayama T, Moinzadeh P, Mechitov KA, Ushita M, Makihata N, Ieiri M, Agha GA, Spencer BF Jr, Fujino Y, Seo JW. Reliable multi-hop communication for structural health monitoring. *Smart Structures and Systems* 2010; **6**(5–6):481–504.
23. Pei JS, Kapoor C, Graves-Abe TL, Sugeng YP, Lynch JP. An experimental investigation of the data delivery performance of a wireless sensing unit designed for structural health monitoring. *Structural Control and Health Monitoring* 2010; **15**:471–504.
24. Rice JA, Mechitov KA, Sim SH, Spencer BF Jr, Agha GA. Enabling framework for structural health monitoring using smart sensors. *Structural Control and Health Monitoring* 2011; **18**:574–587.
25. Udwadia FE, Sharma DK. Some uniqueness results related to building structural identification. *SIAM Journal on Applied Mathematics* 1978; **34**(1):104–118.
26. Udwadia FE. Methodology for optimum sensor locations for parameter identification in dynamic systems. *Journal of Engineering Mechanics* 1994; **120**(2):368–390.

DOI: 10.1002/stc

27. Heredia-Zavoni E, Esteva L. Optimal instrumentation of uncertain structural systems subject to earthquake ground motions. *Earthquake Engineering and Structural Dynamics* 1998; **27**(4):343–362.
28. Kammer DC. Sensor placement for on-orbit modal identification and correlation of large space structures. *AIAA Journal of Guidance, Control, and Dynamics* 1991; **14**(2):251–259.
29. Hemez FM, Farhat C . An energy based optimum sensor placement criterion and its application to structure damage detection. *IMAC*, Honolulu, HI, 1994; 1568–1575.
30. Papadimitriou C, Beck JL, Au SK. Entropy-based optimal sensor location for structural model updating. *Journal of Vibration and Control* 2000; **6**(5):781–800.
31. Abdullah MM, Richardson A, Hanif J. Placement of sensor/actuators on civil structures using genetic algorithms. *Earthquake Engineering and Structural Dynamics* 2001; **30**(8):1167–1184.
32. Guo HY, Zhang L, Zhang LL, Zhou JX. Optimal placement of sensors for structural health monitoring using improved genetic algorithms. *Smart Materials and Structures* 2004; **13**(3):528–534.
33. Cobb RG, Liebst BS. Sensor placement and structural damage identification from minimal sensor information. *AIAA Journal* 1997; **35**(22):369–374.
34. Shi ZH, Law SS, Zhang LM. Optimum sensor placement for structural damage detection. *Journal of Engineering Mechanics* 2000; **126**(11):1173–1179.
35. Chintalapudi K, Fu T, Paek J, Kothari N, Rangwala S, Caffrey J, Govindan R, Johnson E, Masri S. Monitoring civil structures with a wireless sensor network. *IEEE Internet Computing* 2006; **10**(2):26–34.
36. Clark BN, Colbourn CJ, Johnson DS. Unit disk graphs. *Discrete Mathematics* 1990; **86**(1–3):165–177.
37. Tmote Sky sensor node platform. Available from: http://www.ti.com/tool/msp430-3p-motei-tmotesky-dsgkt [Accessed on July 6, 2012].
38. Micaz sensor node platform. Available from: http://bullseye.xbow.com:81/Products/Product_pdf_files/Wireless_pdf/MICAz_Datasheet.pdf [Accessed on July 6, 2012].
39. Juang JN, Pappa RS. An eigensystem realization algorithm for modal parameter identification and model reduction. *Journal of Guidance, Control, and Dynamics* 1985; **8**(5):620–627.
40. CC2420 Radios. Available from: http://www.ti.com/product/cc2420 [Accessed on July 6, 2012].
41. Texas Instrument MSP430. Available from: http://www.ti.com/lsds/ti/microcontroller/16-bit_msp430/overview.page, accessed July 6, 2012.

DOI: 10.1002/stc